MULTI DEGREE OF FREEDOM HINGE JOINTS EMBEDDED ON TUBES FOR

MINIATURE STEERABLE MEDICAL DEVICES

A Thesis

by

SHIVANAND PATTANSHETTI

Submitted to the Office of Graduate and Professional Studies of
Texas A&M University
in partial fulfillment of the requirements for the degree of

MASTER OF SCIENCE

Chair of Committee,   Seok Chang Ryu
Committee Members,   Michael Moreno
                                   Won-Jong Kim
Head of Department,   Andreas A. Polycarpou

August 2017

Major Subject: Mechanical Engineering

ABSTRACT

With the proliferation of successful minimally invasive surgical techniques, comes the challenge of shrinking the size of surgical instruments further to facilitate use in applications such as neurosurgery, pediatric surgery, and needle procedures. The present thesis introduces laser machined, multi-degree-of-freedom (DoF) hinge joints embedded on tubes, as a possible means to realize such miniature instruments without the need for any assembly.

A method to design such a joint for an estimated range of motion is explored by using geometric principles. A geometric model is developed to characterize the joint and relate it to the laser machining parameters, design parameters, and the workpiece parameters. The extent of interference between the moving parts of the joint can be used to predict the range of motion of the joint for rigid tubes and for future design optimization. The total usable workspace is estimated using kinematic principles for joints in series and for two sets of orthogonal joints.

The predicted range of motion was compared to the measured values for fabricated samples of different hinge sizes and kerf dimensions, and it was shown that the predicted values are close to the measured ranges across samples. The embedded hinge joints described in this thesis could be used for micro-robotic applications and minimally invasive surgical devices for neurosurgery and pediatric surgery. Our work can open up avenues to a new class of miniature robotic medical devices with hinge joints and a usable channel for drug delivery.

DEDICATION

Dedicated to the community of researchers in the field of medicine, so that healthcare is

made more accessible and affordable.

ACKNOWLEDGMENTS

CONTRIBUTORS AND FUNDING SOURCES

θ_i	Joint angle of the i-th hinge joint numbered in ascending order from the most proximal to the most distal.
a_i	Link length between $hinge_i$ and $hinge_{i+1}$.
ϕ	Kerf angle made by laser machining at the boundary with the direction of the laser beam.
d_o	Outer diameter of the tubular workpiece.
d_i	Inner diameter of the tubular workpiece.
t	Wall thickness of the tubular workpiece. $\left(t = \frac{d_o - d_i}{2}\right)$
d_c	*Critical section* diameter at which the hinge *pin* looks circular when viewed through the joint axis. If the hinge is designed to look circular on the outer surface, then $d_c = d_o$.
d_h	Hinge diameter when the *critical section* of the hinge is projected as a circle along the joint axis.
ρ	Distance of an arbitrary cylindrical slice of the *pin* or *socket* from the workpiece axis.
k	Kerf width of laser machining at the *critical section*.
$\bar{t}$	Normalized wall thickness. $\left(\bar{t} = \dfrac{t}{d_o}\right)$
$\bar{d}_h$	Normalized hinge diameter. $\left(\bar{d}_h = \dfrac{d_h}{d_o}\right)$
$\bar{k}$	Normalized kerf width. $\left(\bar{k} = \dfrac{k}{d_o}\right)$
b	Hinge axis offset from the rim of the tube segment that contains the *socket*.
β	Angle of the XY projection of the position vector of an arbitrary point P with respect to the YZ plane.

ψ	Angle of the XZ projection of the position vector of an arbitrary point P with respect to the XY plane.
ψ_c	Angular location of a point on the traveling laser kerf cone.
γ	$\sin^{-1}[b/(\frac{d_h}{2})]$.
d_n	Radial location of a point from the hinge center.
χ	Dimensionless parameter indicating the radial location of a point from the hinge center. $\left(\chi = \frac{d_n}{d_h}\right)$
ν	Dimensionless width parameter which is essentially the width of the hinge at a particular angular location ψ, but normalized with respect to the critical section diameter. $\left(\nu = \frac{d_h}{d_c}\cos(\psi)\right)$

TABLE OF CONTENTS

Page

LIST OF FIGURES

1. INTRODUCTION

There has been extensive research on the use and design of steerable needles in medical procedures, most of which has been about solid metallic wires with beveled tips [1], [2], [3]. A robot arm holds and manipulates the needle's proximal end to send its distal tip to the site of interest, followed by the insertion of a flexible polymer sheath over the wires to create a working channel. This procedure is called the Seldinger technique [4]. In spite of the fact that this passive needle steering has invigorated surgical robotics for the last decade, a few significant technical challenges still remain due to the indirect tip control approach. A complicated mechanics model between the proximal and the distal tip is required inside inhomogeneous tissue even for simple procedures, and a higher curvature turning is not available.

An active needle design was introduced [5] to address the issues, in which a flexure joint was laser machined near the needle tip, enabling direct and active tip orientation control. Since the active needle, the other needle-size steerable device have been proposed following the tip joint concept, for example, a miniature robotic wrist embedment in [6] and various tip steerable needle designs [7], [8], [9], [10]. They consist either of flexure based planar joints or ball joints. Both of these types pose a challenge with respect to the precise and dexterous tip control of miniature medical devices. In the former case, the limited degree-of-freedom (DoF) reduces the device dexterity, while the latter necessitates precise alignment of sub-components and assembly, requiring high manufacturing cost and preventing further miniaturization. It is highly desired to develop a sophisticated fabrication method of joints with more intuitive kinematics and high maneuverability (not needing a large space to turn or orient).

Filip Jelinek et. al [11] provided a comprehensive overview of such joints along with

a method of classification into *rolling*, *sliding*, *rolling-sliding* and *bending*. The 8-mm diameter EndoWrist arm driven by cables and pulleys (Intuitive Surgical, Sunnyvale, CA), is an example of a rolling joint. Notable examples are described by [12], [13], and [14]. For extremely small robotic manipulators, those rolling joints have the disadvantage of requiring micro-alignment and micro-assembly. An example of a bending joint is a needle with asymmetrically machined slits to make it compliant in bending, like the one featured by [5] and [15], but they are prone to fatigue due to repeated actuation and have a limited dexterity. It is also unintuitive to precisely control the positioning of the end effector or tip because of the highly non-linear behavior of NiTi materials. US Patent 7766821 [16] describes an articulate tube made of multiple segments connected to one another by a sliding joint, each of which functions as a planar pivot. The sliding joints with laser machined hinges (like those mentioned in [16]) may mitigate the above listed issues. They also permit an inner channel when they are embedded on tubes, useful for drug delivery or fluid exchange. However, multi-segmented snake like wrists as found in the 5-mm diameter Da Vinci Instruments [17] [18] make precise control less intuitive like the bending joints, the longer they get. Moreover, longer joints have a decreased workspace compared to a simple hinge joint to reach a target [19] and shorter or fewer segment joint facilitates the estimation of the end effector position. For this, replacing the bending joint with a sliding hinge joint and reducing the number of segments by maximizing the range of motion of each segment may allow for better and intuitive estimates of the end effector position and extend the device workspace, given the actuation effort.

Hence it is clear that laser machined hinge joints on tubes can potentially be used in minimally invasive surgery due to their inherent advantages: there is no need for assembly, multi-DoF motion is possible when appropriately arranged, an inner channel can be preserved for matter exchange, fatigue is reduced because sub-components do not need to bend too much and the joints can be controlled more intuitively and precisely because

Figure 1.1: Examples of multi-DoF hinge joints embedded on miniature tubes by on-axis laser machining. From the left, an 8 mm diameter EndoWrist arm used in the da Vinci surgical robotic system (added for the size comparison), a 5 mm diameter Stainless Steel tube with 2-2 orthogonal hinge joints, a 1.27 mm diameter NiTi tube with 3-3 orthogonal hinge joints, and a 1.27 mm diameter NiTi tube with 1-1 orthogonal hinge joints.

the end effector basically pivots about the hinge joints. The inner channel, especially, can be used as a platform to deliver new medical treatments (laser surgery [20], plasma [21] and cell-based treatment [22]). Currently, the instruments that do require a high level of bending compliance are made of NiTi alloy [23] (due to its superelasticity) which is considerably more expensive than stainless steel. The proposed hinge joint allows for the use of a stronger and affordable material since it is only a sliding joint and thereby there is low fatigue. This material change will significantly save the manufacturing cost, leading to the full design customizability to suit specific surgical procedures and even individuals.

This thesis will propose a method for the design and fabrication of laser-machined, multi-DoF embedded hinge joints on tubular devices (Fig. 1.1), without needing any assembly, while the inner channel remains usable for drug delivery and exchange of fluids.

It illustrates a geometric model of the joint, incorporating the nature of on-axis laser machining. The model is then used to estimate the range of motion of the joint design for a particular set of parameters toward the future optimization process. Distinct configurations of these hinge joints are presented to achieve different degrees of usable workspace.

One can note that a joint as proposed above, is only indispensable for small tubular devices. The larger such device, the easier it is to assemble a hinge joint. But with increasing miniaturization, such assembly becomes increasingly uneconomical and time-consuming. Hence, the joint proposed here is targeted at devices smaller than 5mm in diameter (5mm is currently the size of the smallest Intuitive Surgical EndoWrist® tools).

2. BACKGROUND

Laser machining can be used to cut a variety of materials by generating a high heat flux which melts and vaporizes the material at which it is directed (see Fig. 2.1). Manufacturing processes generally use CO_2 and Neodymium Yttrium Aluminum Garnet (Nd:YAG) lasers. Compared to CO_2 lasers, Nd:YAG lasers have a shorter wavelength of about 1 μm which makes them better suited for cutting reflective materials like metals due to their higher absorption [24]. Laser machining is popular due to low material wastage, no tool wear, small kerf width, and high accuracy. Laser machining typically results in a small taper angle [25], hereafter called the kerf angle.

To be able to fabricate a non-assembled stable hinge joint which does not dislocate along the pivot axis (the axis about which the hinge joint actuates), the '*pin*' of the hinge must wedge into the '*socket*' of the hinge. This is achieved by running the laser beam radially around the workpiece (a tube) such that the laser beam always passes through the axis of the tubular workpiece while being normal to the tube axis. Hence the cutting motion of the laser beam consists of two parts superimposed: lengthwise cutting (which involves the workpiece moving along the tube axis) and radial cutting (which involves the workpiece rotating about its axis) [16]. Henceforth, the radial laser cutting described above will be referred to as 'on-axis' laser machining (Fig. 2.2(b)) to distinguish it from off-axis machining where a laser beam can run askew from the tube axis and not pass through it.

Besides the listed advantages, the on-axis laser machined hinge joint also has some limitations. The range of motion of the joint is influenced by the geometry of the joint, with a trade off between stability (resistance to dislocation of the joint) and range. The stability of the hinge is also dependent on parameters like the hinge size, kerf size and thickness of
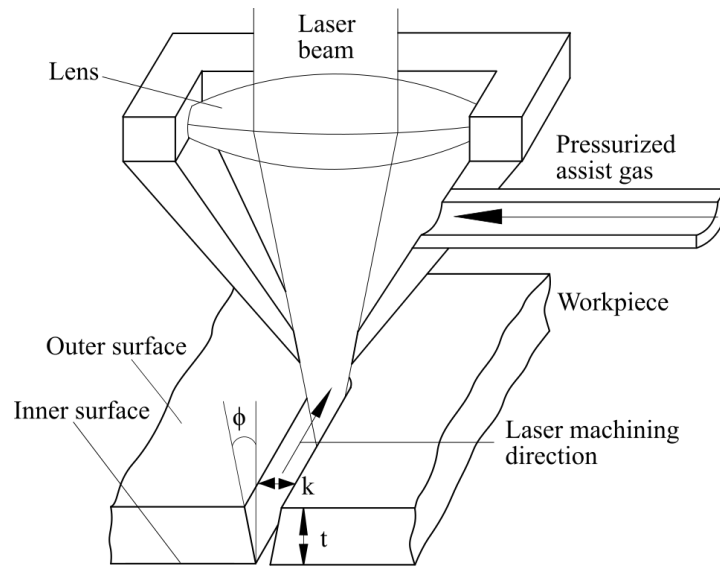
Figure 2.1: The process of laser machining. A beam of laser is focused onto the desired location on the workpiece while being fed continuously with a pressurized assist-gas. In this thesis, the effect of laser cutting will be simplified and studied by incorporating a kerf-angle (ϕ) and kerf width (k)

(a) Off-axis   (b) On-axis   (c) On-point
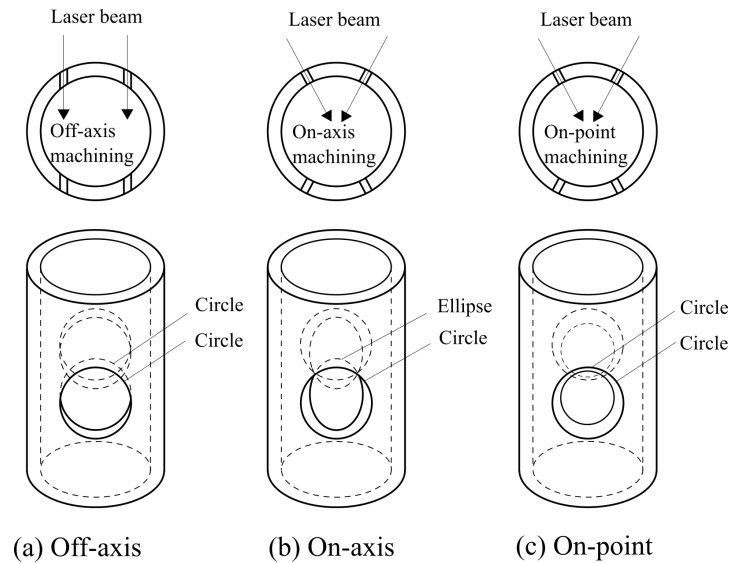
Figure 2.2: Comparison of (a) off-axis, (b) on-axis, and (c) on-point machining for cutting hinge joints. Different hinge geometries can be achieved by suitably directing the laser beam. On-axis and on-point machining result in the formation of a wedge that prevents the hinge from moving into the workpiece. This wedging action can secure the hinge against lateral dislocation when machined on both sides of the workpiece. In this thesis, on-axis machining is examined.

6

the workpiece which can either increase or decrease the resistance to dislocation. There is also the risk of material failure if the hinge is forced to actuate beyond the range its geometry allows.

The problem of mechanical interference between the *pin* and *socket* could be solved by shaping the *pin* like a conical frustum. We will call this type of machining as *on-point* machining. It will no longer be a case of elliptical sections rotating in elliptical sections (hence there is no interference). However, a laser machine with at least four degrees of freedom is needed to achieve this (two rotational degrees and two translational degrees of freedom). In addition to being more expensive, fabrication of such a hinge would require a more complicated toolpath planning. Accordingly, this thesis will study the on-axis laser machined hinge joints.

3. OBJECTIVES

The purpose of this thesis is to specify design guidelines for using on-axis laser machining as a means to embed hinge joints on tubular workpieces. Equations are derived for planning toolpaths to cut a general 3D curve on a tube, followed by equations to plan toolpaths for the constituent parts of a hinge. A geometric model is derived for the proposed hinge joint, and its range of motion is predicted for various combinations of design and manufacturing parameters. This is validated for 3 samples fabricated with different hinge sizes. Finally, an estimate of the reachable workspace is provided for various hinge configurations. The objectives are:

1. Design: Provide methods for designing the hinge and the neck, and the fabrication process, for on-axis laser machining.

2. Geometric Model: Derive a geometric model for the hinge joint in 3D, to support the idea that on-axis machining can indeed create a stable wedged hinge geometry.

3. Range of Motion: Predict the range of motion of the joint (for rigid tubes) based on the geometric model, as different parameters are varied. Experimentally validate the motion range for samples fabricated in three different hinge sizes.

4. Workspace: Present an analysis of the reachable workspace of various configurations of hinges.

There are however, limitations to this analysis. The effect of the laser machining process has been simplified, ignoring the influence of the heat affected zone and manufacturing imperfections. The effect of material wear on repeated actuation is not considered. The concept of 'range-of-motion' is not rigidly applicable to the hinge joint presented in this

thesis. Due to the mechanical interference at the interface of the *pin* and *socket*, the joint offers progressively higher resistance till either the adjacent tube segment stops further actuation, or the material fails. Nevertheless, it still provides us a safe range of actuation to prevent wear and damage to the joint.

The embedded hinge joints that will be illustrated in this thesis could be used for micro-robotic applications and minimally invasive surgical devices (especially for diameters less than 5mm) for neurosurgery and pediatric surgery. They can also be used in robotic arms with an inner space for electronics and sensing equipment.

4. DESIGN AND FABRICATION

The embedded laser-machined hinge joint has three main design elements- the *pin*, the *socket*, and the *neck* as shown in Fig. 4.1. The actuation of the joint comprises of a circular piece of tube (the *pin*) rotating inside a rounded cut on the tube (the *socket*). Tapered walls flank the *pin*, to permit an extent of joint actuation without the tube segments hitting each other. In this thesis, we consider embedding such a hinge joint onto a steerable cannula with a sharp tip, as shown in Fig. 4.1. Though we designed the prototype with slots for tendon actuation, detailed treatment of the topic is beyond the scope of this thesis.

A regular on-axis laser machining equipment has two different motions. It can spin a tubular workpiece about the axis, as well as translate it along the axis. To lay toolpaths for the machine, a 2D sketch is usually prepared by unwrapping the design that is to be carved. The laser machine cuts along these toolpaths, as though the sketch is radially wrapped around a cylinder.

For the purpose of this analysis, let there be a coordinate system as in Fig. 4.2(a). The origin is at the center of the distal hinge, on the axis of the hinge and the Z axis is along the axis of the tube. Let $z = f(x, y)$ be a desired 3D curve on the workpiece (as in Fig. 4.2(a)). Suppose this curve exists on an imaginary cylindrical section at radius $d_c/2$. We will henceforth call this section, on which the curves to be cut are designed, as the *critical section*. The Z axis is mapped to the $\bar{Y}$ axis, while the X and Y axes are mapped onto the $\bar{X}$ axis of the sketch (see Fig. 4.2(a) and 4.4). Let P be a point on the 3D curve. Its x and y coordinates can be replaced by $\frac{d_c}{2}\sin(\beta)$ and $\frac{d_c}{2}\cos(\beta)$ respectively, where β is the angle of the XY projection of the position vector of P with respect to the YZ plane (Fig. 4.3). Since the *critical section* unwraps to form the sketch, the circumference of that circle would correspond to a line parallel to the $\bar{X}$ axis. β would hence satisfy $\beta\frac{d_c}{2} = \bar{x}$. The

10
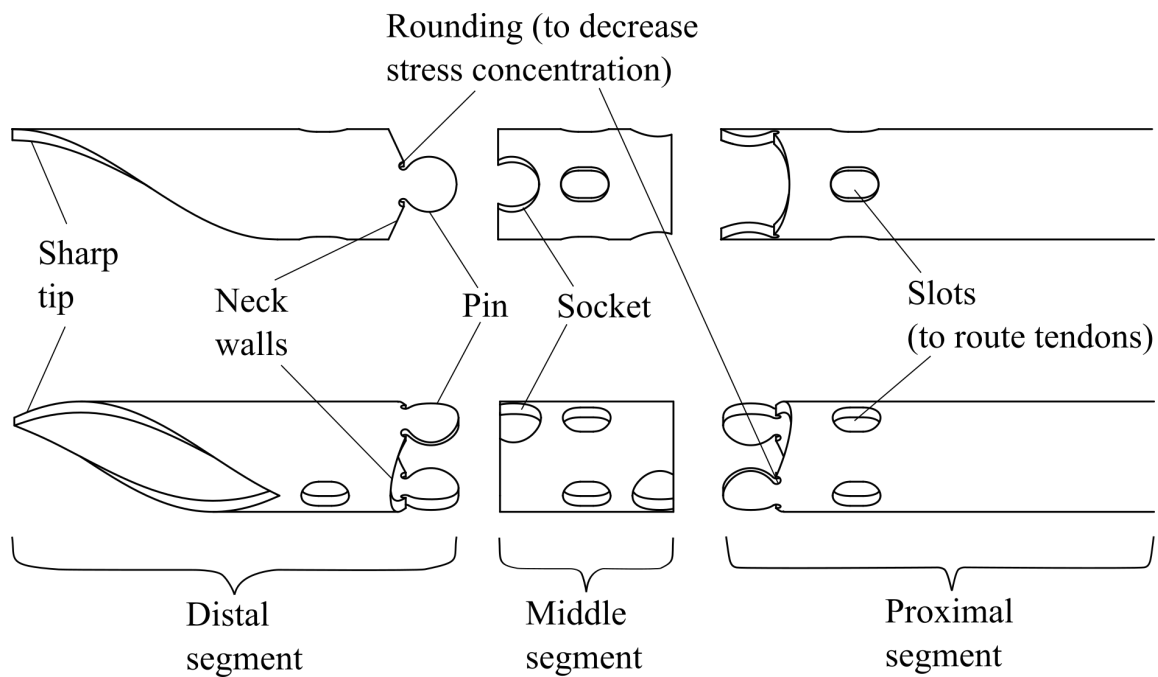
Figure 4.1: Laser-machined hinge joints embedded on a tube to form a 2 DoF steerable cannula showing an exploded view with the various parts labeled (Note: The joints do not need any assembly)
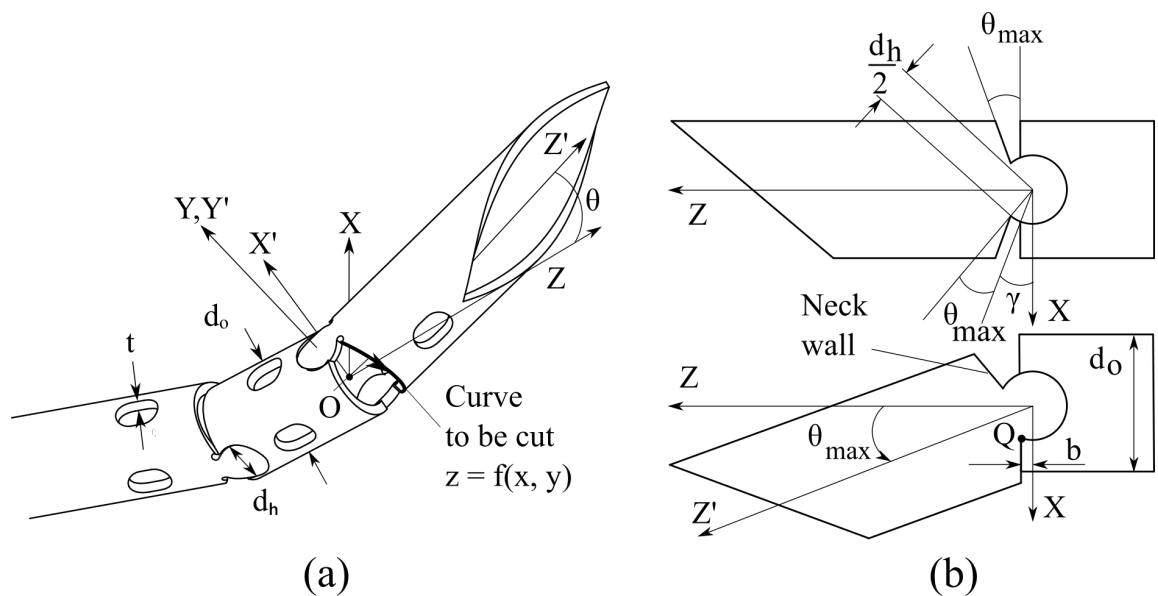
Figure 4.2: Laser-machined hinge joints embedded on a tube to form a 2 DoF steerable cannula showing (a) the actuated configuration with the local coordinate system and geometric parameters. One of the machined curves is labeled, and has the equation $z = f(x, y)$. (b) Design of the *neck* based on the intended range of motion.
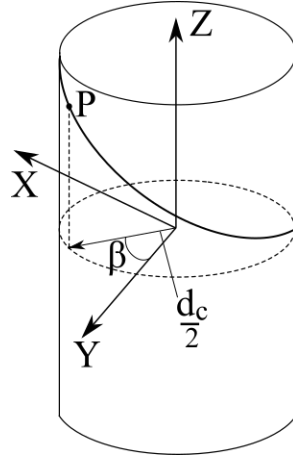
Figure 4.3: Unwrapping from an arbitrary point P on the curve z = f(x, y)

equation of the above curve on a 2D sketch would then be:

$$\bar{y} = f\left[\frac{d_c}{2}\sin\left(\frac{\bar{x}}{d_c/2}\right), \frac{d_c}{2}\cos\left(\frac{\bar{x}}{d_c/2}\right)\right] \tag{4.1}$$

where $\bar{x}$ and $\bar{y}$ are the mapped 2D Cartesian coordinates on the sketch prepared for generating toolpaths.

It is thus clear that, to map a 3D curve of cut to an unwrapped 2D sketch whose $\bar{Y}$ is aligned with the Z axis, (x, y, z) are to be replaced by $\left\{\frac{d_c}{2}\sin\left(\frac{\bar{x}}{d_c/2}\right), \frac{d_c}{2}\cdot\cos\left(\frac{\bar{x}}{d_c/2}\right), \bar{y}\right\}$.

4.1 Hinge design

The hinge is designed to have a circular shape at the *critical section*. Let the equation of this circle in 3D be: $(x, z) = \left\{\frac{d_h}{2}\cos(\psi), \frac{d_h}{2}\sin(\psi)\right\}$, where ψ is an angular parameter. This can be mapped to a 2D curve by substituting appropriately as detailed above. The mapped equation is:

$$(\bar{x}, \bar{y}) = \left\{\frac{d_c}{2}\sin^{-1}\left(\frac{d_h}{d_c}\cos(\psi)\right), \frac{d_h}{2}\sin(\psi)\right\} \tag{4.2}$$

The above equation is used to cut the curved part of the hinge. If d_c is made equal to d_o, the hinge would look like a circle on the outer surface of the tube. However, if d_c is made equal to d_i, the hinge will look like a circle on the inner surface. So the *critical section* can be moved to any section between the inner to outer surfaces of the tube. Nevertheless, the hinge takes on an elliptical shape at all other cylindrical sections due to the nature of on-axis machining.

The hinge joint as presented in this thesis has two distinct parts - the inner *pin* and the outer enclosing *socket*. Since the laser kerf is not negligible for smaller sized workpieces, the hinge *pin* will be slightly smaller than the planned hinge size and the hinge *socket* will be slightly larger. This forms a gap which allows the hinge to move.

4.2 Neck design

The *neck* of the tube segment that is attached to the *pin*, can be designed to allow a particular intended range of motion. Let the *neck* consist of a tapering column with the *pin* at one end, as shown in Fig. 4.2(b). Assume that at the sloping walls of the column are flat and that one of the walls is to be in contact with the rim of the adjacent tube segment at the end of the joint motion. In this case, one can calculate the slope of the *neck* walls. Let θ_{max} be the intended range of the joint on one side. When the joint is actuated by θ_{max}, a point of contact Q at the corner of the *socket*, on the adjacent tube segment is given by: $Q(x, z) = \left\{ \frac{d_h}{2} \cos(\gamma + \theta_{max}), \frac{d_h}{2} \sin(\gamma + \theta_{max}) \right\}$, where $\gamma = \sin^{-1} \left[\dfrac{b}{\left(\frac{d_h}{2}\right)} \right]$. The wall also has a slope of $\tan(\theta_{max})$. Using the point slope form,

$$z - \frac{d_h}{2} \sin(\gamma + \theta_{max}) = \tan(\theta_{max}) . \left[x - \frac{d_h}{2} \cos(\gamma + \theta_{max}) \right]$$

Any equation $z = f(x,y)$ transforms into equation 4.1. Applying the same transformation,

$$\bar{y} - \frac{d_h}{2}\sin(\gamma + \theta_{max}) = \tan(\theta_{max}).\left[\frac{d_c}{2}\sin\left(\frac{\bar{x}}{d_c/2}\right) - \frac{d_h}{2}\cos(\gamma + \theta_{max})\right].$$

The equation of the 2D line sketch to cut the *neck* is hence:

$$\tan(\theta_{max}) = \frac{\bar{y} - \frac{d_h}{2}\sin(\gamma + \theta_{max})}{\frac{d_c}{2}\sin(\frac{\bar{x}}{d_c/2}) - \frac{d_h}{2}\cos(\gamma + \theta_{max})} \tag{4.3}$$

The above equation allows adjustment of *neck* slope based on the intended range of motion of the joint. This can help avoid excessively large gaps on the sides of the joint, and also provide a physical stop to prevent over-actuation.

4.3 Fabrication

The process of embedding hinge joints on a tube consists of the following steps:

1. Prepare a sketch of the pattern to be machined: The sketch will be a design which the laser machine wraps around the workpiece for machining. The curves on the sketch representing the hinges and *neck* walls are drawn using equations 4.2 and 4.3 respectively. Other features like slots, end cuts and bevel tips are similarly derived from the general equation 4.1. Figure 4.4 shows a sample sketch to embed two orthogonal hinges on a 1.27mm diameter workpiece.

2. Lay out toolpaths to cut the above sketch using a suitable CAM software. The tool size is generally equal to the laser kerf width. The process of laying toolpaths is identical to that of an end-milling application.

3. Generate G-code for the laser machine using a post processor. Select laser parameters based on the workpiece material, geometry, and laser type.
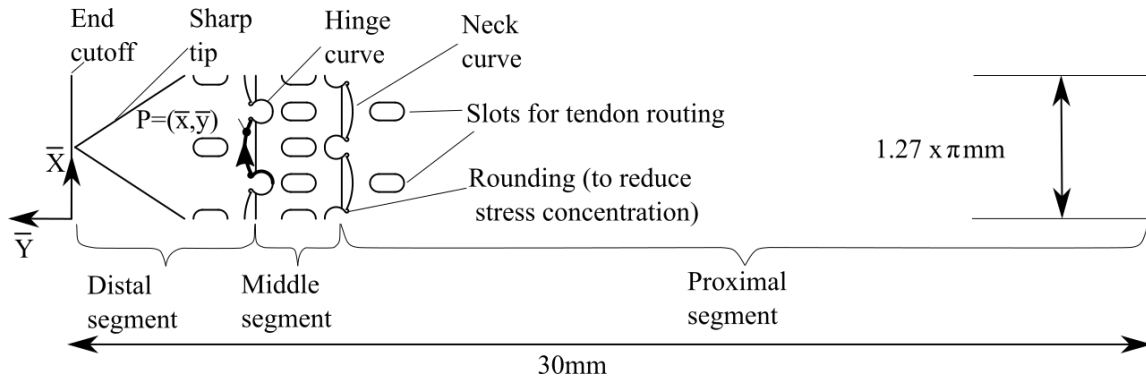
Figure 4.4: A sample sketch to embed two orthogonal hinge joints onto a 30 mm long tube of diameter 1.27 mm. Slots are made to allow tendon routing. The hinge and *neck* curves are derived from equations 4.2 and 4.3 respectively.

4. Run the G-code on the laser machine to cut the sample. Supply assist gas and cooling fluids as needed.

4.4 Inner Tube Size

The inner channel in the fabricated sample can be used for various purposes such as drug delivery and fluid drainage. However, to enable this, an inner tube must exist for the smooth passage of matter, and to prevent leakage. But this presents a challenge since the outer metallic tube does not have a continuous bent profile. The maximum inner tube diameter can be calculated for a particular workpiece bore and range of joint actuation, so that the tube is not pinched (see Fig. 4.5). The minimum distance from point O' to the line PQ (on the inner surface of the workpiece with embedded hinge joint) is taken as the upper limit on the inner tube diameter.

Let the equation of the line PQ be $z = mx + c$ at the maximum actuation angle θ_{max} where m, the slope, is $tan(90° - \theta_{max})$ and c is the Z intercept. This line passes through the point $(x, z) = \left\{ \dfrac{-d_i}{2}, 0 \right\}$ as it is at a distance $\dfrac{-d_i}{2}$ from the Z axis when the joint is not actuated. Substituting the former into the line equation,
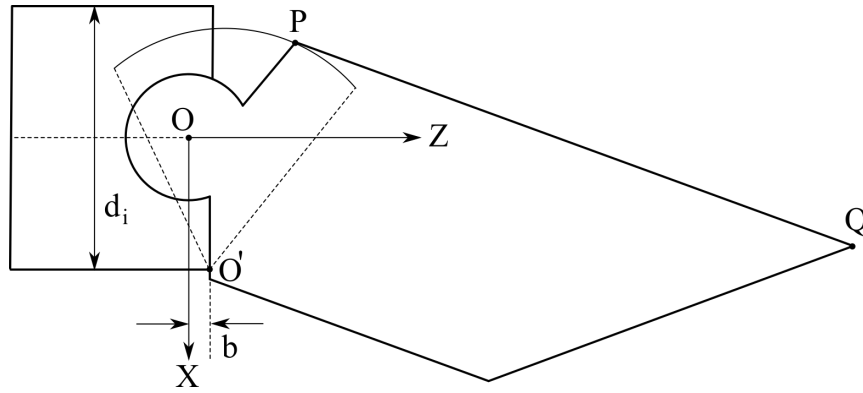
Figure 4.5: A schematic showing the actuated position of the joint at the end of its range of motion. The maximum inner tube radius is lesser than that of the workpiece as the workpiece does not have a continuous bent profile. The minimum distance from point O' to the line PQ is taken as the upper limit on the inner tube diameter

$$z = mx + c \text{ , and } (x, z) = \left\{ \frac{-d_i}{2}, 0 \right\}$$

$$\implies 0 = m.\left(\frac{-d_i}{2} \right) + c$$

$$\implies c = m.\left(\frac{d_i}{2} \right)$$

The equation of line PQ hence becomes

$$z = mx + m.\left(\frac{d_i}{2} \right)$$

$$\implies z = m.\left(x + \frac{d_i}{2} \right)$$

The minimum distance of point $O' = \left(\dfrac{d_i}{2}, b\right)$ from the above line is given by:

$$
\begin{aligned}
&= \frac{\left| m.\left(x + \dfrac{d_i}{2}\right) - y \right|}{\sqrt{m^2 + 1}} \\
&= \frac{\left| m.\left(\dfrac{d_i}{2} + \dfrac{d_i}{2}\right) - b \right|}{\sqrt{m^2 + 1}} \\
&= \frac{|m.d_i - b|}{\sqrt{m^2 + 1}} \\
&= \frac{|tan(90 - \theta_{max}).d_i - b|}{\sqrt{(tan(90 - \theta_{max}))^2 + 1}}
\end{aligned}
$$

Hence, the upper limit on the inner tube diameter is $d_{innertube} = \dfrac{|tan(90 - \theta_{max}).d_i - b|}{\sqrt{(tan(90 - \theta_{max}))^2 + 1}}$

4.5 Geometric model of the hinge joint in 3D

A geometric model is helpful to study the behavior of the hinge joint fabricated using on-axis laser machining. For the purpose of the below analysis, the *pin* and *socket* are examined in isolation, without any *neck*.

At any tube section away from the *critical section*, the pin and socket are narrowed or elongated in the X direction depending on whether the section is towards the outside or the inside of the tube respectively. This is a direct consequence of the above-mentioned phenomenon seen in Fig. 2.2 (b).

To cut a circular hinge on the *critical section*, a circle is projected on it. The x and z coordinates of that circle could then be expressed in the parametric form as shown below:

$$
\begin{pmatrix} x \\ z \end{pmatrix} = \left\{ \begin{array}{c} \frac{d_h}{2}\cos(\psi) \\ \frac{d_h}{2}\sin(\psi) \end{array} \right\}
$$

The curve lies on the *critical section*, which is a cylinder with a circular cross-section
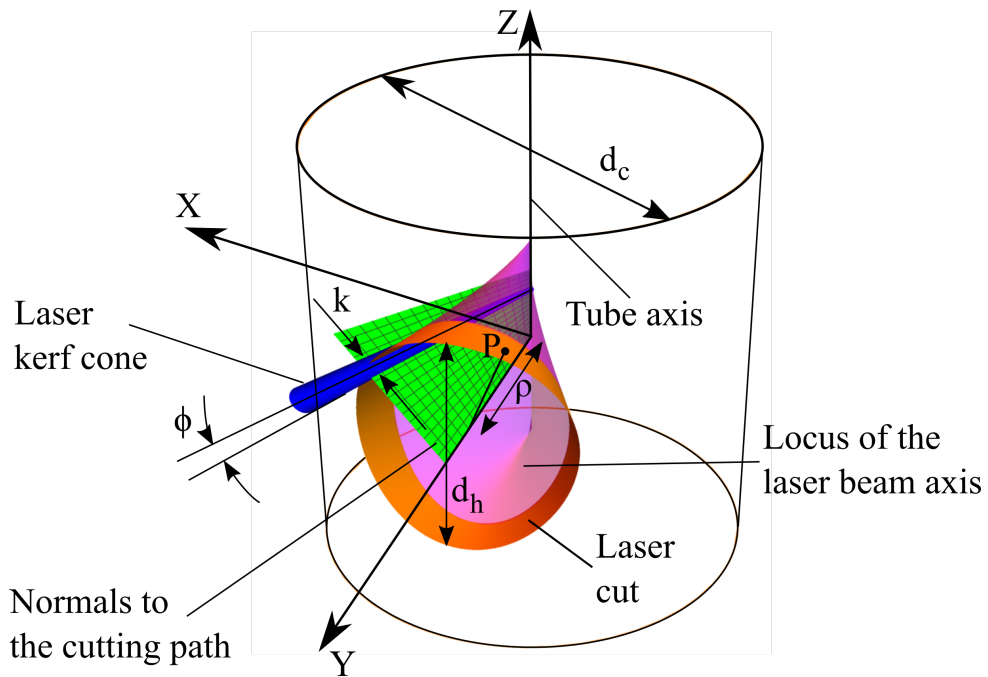
Figure 4.6: The geometric model of the hinge showing the laser cutting path (shown in orange), normals to the laser cutting path (shown in green), the machining kerf cone (shown in blue), and other relevant labeled parameters of interest.
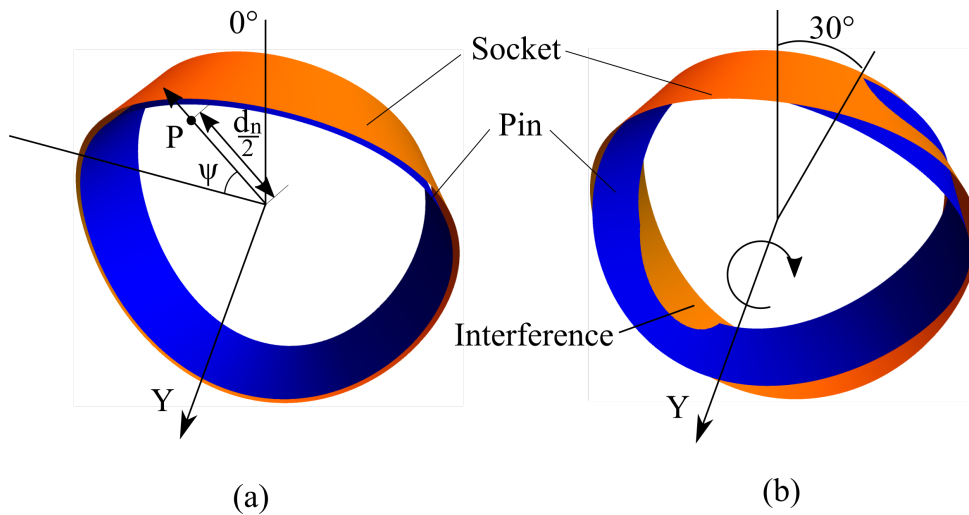
Figure 4.7: (a) Shows the outer *pin* (in blue) and inner *socket (in orange)* surfaces at the *pin-socket* interface. (b) shows the same two *pin* and *socket* surfaces when the pin is rotated by $30°$ about the Y axis.

of diameter d_c. So the x and y coordinates satisfy the equation:

$$x^2 + y^2 = \left(\frac{d_c}{2}\right)^2$$

$$\implies y^2 = \left(\frac{d_c}{2}\right)^2 - x^2$$

$$\implies y^2 = \left(\frac{d_c}{2}\right)^2 - \left[\frac{d_h}{2}\cos(\psi)\right]^2$$

$$\implies y = \sqrt{\left(\frac{d_c}{2}\right)^2 - \left[\frac{d_h}{2}\cos(\psi)\right]^2}$$

The laser beam hence has to meet the *critical section* at the point

$$\vec{P}_{critical}(x, y, z) = \left\{ \frac{d_h}{2}\cos(\psi), \sqrt{\frac{d_c}{2}^2 - \left[\frac{d_h}{2}\cos(\psi)\right]^2}, \frac{d_h}{2}\sin(\psi) \right\} \tag{4.4}$$

where ψ (see fig. 4.7(b)) is an angular parameter. We define the dimensionless width expression $\nu = \frac{d_h}{d_c}\cos(\psi)$ to simplify the repeating terms. ν is essentially the width of the hinge at a particular angular location ψ, but normalized with respect to the critical section diameter. Depending on the angular location on the hinge, ν can range from 0 at the proximal and distal extremes ($\psi = \frac{\pi}{2}, \frac{3\pi}{2}$) of the hinge to a maximum of $\frac{d_h}{d_c}$ (width at the center of the hinge, where $\psi = 0, \pi$), which is the hinge diameter normalized with respect to the critical section diameter. So the width of the hinge at any radius ρ (see Fig. 4.6) from the tube axis is given by $\rho\nu$. The equation for the laser beam trajectory is obtained in terms of the above radius ρ and dimensionless hinge width ν by considering that each point on the laser beam lies on a hypothetical circle of radius ρ and converges at the tube

axis. This is accomplished by scaling the x and y coordinates of equation 4.4 by $\dfrac{\rho}{d_c/2}$:

$$\vec{P}_{trajectory}(x,y,z) = \left\{ \frac{\rho}{d_c/2} \cdot \frac{d_h}{2} \cos(\psi), \frac{\rho}{d_c/2} \cdot \sqrt{\frac{d_c}{2}^2 - \left[\frac{d_h}{2}\cos(\psi)\right]^2}, \frac{d_h}{2}\sin(\psi) \right\}$$

$$= \left\{ \rho\frac{d_h}{d_c}\cos(\psi), \rho \cdot \sqrt{1 - \left[\frac{d_h}{d_c}\cos(\psi)\right]^2}, \frac{d_h}{2}\sin(\psi) \right\}$$

$$\implies \vec{P}_{trajectory}(x,y,z) = \left\{ \rho\nu, \rho\sqrt{1-\nu^2}, \frac{d_h}{2}\sin(\psi) \right\} \tag{4.5}$$

We introduce a factor $\chi = \dfrac{d_n}{d_h}$, where d_n (see Fig. 4.7(a)) indicates the radial location of a point from the hinge center. $\chi = 0$ at the center of the hinge (Y axis), whereas χ has a maximum of 1 on the outer boundary of the hinge (the *pin-socket* interface). The normals to the trajectory are obtained by considering that they are perpendicular to the tangents of the laser trajectory and that the normals pass through the Y axis.
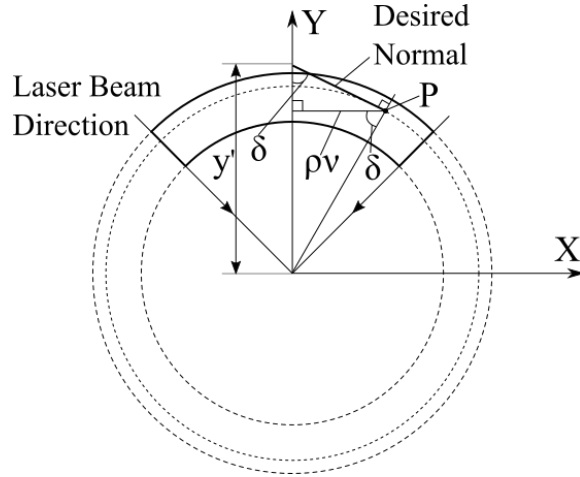
Figure 4.8: Cross-sectional view of the hinge at its widest, showing the parameters involved in finding the equation of the normal to the laser path. Point P is on the boundary of the hinge, but in a different plane, hence being closer to the center than the laser beam directions shown at the hinge boundaries for the plane at which the hinge is widest.

Let x_{normal}, y_{normal}, and z_{normal} be the coordinates of a point on the normal to the laser trajectory. From figure 4.8,

At $d_n = d_h$, $x_{normal} = \rho\nu$ and $y_{normal} = \rho\sqrt{1-\nu^2}$.

At $d_n = 0$, $x_{normal} = 0$ and $y_{normal} = y'$ (see fig. 4.8)

From the figure, $y' = \rho\nu \left(\tan\delta + \dfrac{1}{\tan\delta} \right)$

But $\tan\delta = \dfrac{y_{normal}}{x_{normal}} = \dfrac{\rho\sqrt{1-\nu^2}}{\rho\nu}$.

$$\text{Therefore, } y' = \rho\nu \left(\frac{\sqrt{1-\nu^2}}{\nu} + \frac{\nu}{\sqrt{1-\nu^2}} \right)$$
$$= \rho\nu \left(\frac{1-\nu^2+\nu^2}{\nu\sqrt{1-\nu^2}} \right)$$
$$= \frac{\rho}{\sqrt{1-\nu^2}}$$

Using linear interpolation, $x_{normal} = 0 + \left(\dfrac{d_n}{2} - 0 \right) \left\{ \dfrac{\rho\nu - 0}{\frac{d_h}{2} - 0} \right\} = \dfrac{d_n}{d_h}\rho\nu = \chi\rho\nu.$

Similarly,

$$y_{normal} = \frac{\rho}{\sqrt{1-\nu^2}} + \left(\frac{d_n}{2} - 0 \right) \left\{ \frac{\rho\sqrt{1-\nu^2} - \dfrac{\rho}{\sqrt{1-\nu^2}}}{\dfrac{d_h}{2} - 0} \right\}$$

$$= \frac{\rho}{\sqrt{1-\nu^2}} + \frac{d_n}{d_h}\rho \left\{ \frac{1-\nu^2-1}{\sqrt{1-\nu^2}} \right\}$$

$$= \rho \left\{ \frac{1}{\sqrt{1-\nu^2}} - \frac{d_n}{d_h}\frac{\nu^2}{\sqrt{1-\nu^2}} \right\}$$

$$= \frac{\rho}{\sqrt{1-\nu^2}} \left\{ 1 - \frac{d_n}{d_h}\nu^2 \right\}$$

$$= \frac{\rho(1-\chi\nu^2)}{\sqrt{1-\nu^2}}$$

The z coordinate of the normal to the laser trajectory will be the z coordinate of the

point on the trajectory scaled by the distance from the hinge center.

$$z_{normal} = \frac{d_n}{d_h}\frac{d_h}{2}\sin(\psi)$$
$$= \chi\frac{d_h}{2}\sin(\psi)$$

The equation of the normal lines to the laser trajectory are hence given by:

$$\vec{P}_{normals}(x, y, z) = \left\{ \chi\rho\nu, \frac{\rho\left(1 - \chi\nu^2\right)}{\sqrt{1 - \nu^2}}, \chi\frac{d_h}{2}\sin(\psi) \right\} \tag{4.6}$$

The laser kerf is modeled as a traveling cone as can be seen in Fig. 4.6 (utilizing the simplified model shown in Fig. 2.1) with base diameter k at the *critical section*, cone angle ϕ, and the trajectory described in eq. 4.5. The equation of the cone is hence:

$$\vec{P}_{cone}(x, y, z) =$$

$$\begin{pmatrix} \rho\nu + \left(\sqrt{1 - \nu^2}\right)\cos(\psi_c)\left[\left(\rho - \frac{d_c}{2}\right)\tan(\phi) + \frac{k}{2}\right] \\ \rho\sqrt{1 - \nu^2} - \nu\cos(\psi_c)\left[\left(\rho - \frac{d_c}{2}\right)\tan(\phi) + \frac{k}{2}\right] \\ \frac{d_h}{2}\sin(\psi) + \sin(\psi_c)\left[\left(\rho - \frac{d_c}{2}\right)\tan(\phi) + \frac{k}{2}\right] \end{pmatrix} \tag{4.7}$$

where ψ_c is a parameter indicating the angular position of a point on the kerf cone boundary.

To find the equations for surfaces of the *pin* and the *socket*, the intersection of the laser trajectory normals (eq. 4.6) with the kerf cone (eq. 4.7) is obtained. Using Mathematica [26] to solve these intersection equations, the *pin* and *socket* surfaces are obtained as functions of joint design parameters (d_h, d_c), laser parameters (k, ϕ) and geometrical parameters (ρ, ψ). Let $\vec{P}_{pin_s} = f_{pin_s}(\rho_{pin}, \psi_{pin}, d_h, d_c, k, \phi)$ represent the parametric equations of the *pin* surface so obtained. Similarly $\vec{P}_{socket_s} = f_{socket_s}(\rho_{socket}, \psi_{socket}, d_h, d_c, k, \phi)$ represents those of the *socket* surface. Then, the interfering points between the *pin* and *socket*

22

surfaces at their interface is:

$$R_Y(\theta) f_{pin_s}(\rho_{pin}, \psi_{pin}, d_h, d_c, k, \phi) =$$

$$f_{socket_s}(\rho_{socket}, \psi_{socket}, d_h, d_c, k, \phi)$$

(4.8)

where θ is the angle by which the pin is rotated with respect to the $socket$ and R_Y indicates the rotation matrix about Y axis.

5. RANGE OF MOTION ANALYSIS

Due to the nature of on-axis machining, the *pin* and *socket* are made up of elliptical bounding curves away from the *critical section*. This wedges the hinge in place to constrain translation and allow rotation. However, it has the unintended effect of restricting rotation beyond a certain angle. Notwithstanding the laser kerf gap, elliptical *pin* sections can only move by a certain angle in an elliptical *socket* before they start to mechanically interfere. This is usually not a problem in thin tubes or tubes made of compliant materials like Nitinol. But for rigid materials like stainless steel, this phenomenon can actually limit the safe range of actuation. Forcing actuation far beyond this limit could damage the hinge.

Two different kinds of mechanical interference can affect the range of actuation :

1. The *neck* of the tube segment containing the *pin* mechanically interferes with the rim of the tube segment containing the *socket*.

2. The *pin* and the *socket* mechanically interfere with each other at their mating interface due to the geometry of on-axis laser machining.

The former can be used deliberately to restrict the range of the joint, as described in section 4.2. The latter is considered in the following part of the section.

The extent of interference depends on θ, the joint design parameters (d_h and d_c), the laser machining parameters (k and ϕ)), and the workpiece geometry parameters (d_o and t). Some of these parameters can be normalized with respect to the outer d_o to give $\overline{d_c}$, $\overline{t}$, $\overline{d_h}$, and $\overline{k}$, which, along with ϕ, characterize the extent of interference.

From the geometric model described in the previous section, the above effects can be approximately characterized. However, there are certain limitations to using it to find

24

the range of motion of on-axis laser machined embedded hinge joints: 1) The concept of 'range' is not rigidly applicable to the hinge joint presented in this thesis. Due to the mechanical interference at the interface of the *pin* and *socket*, the joint offers progressively higher resistance till either the adjacent tube segment stops further actuation, or the material fails. 2) The *pin* is assumed to be at the center of the *socket*, whereas in reality, it can move around due to the kerf gap. 3) The material at the interface of the *pin* and *socket* might wear away on repeated actuation. 4) Defects and variability in manufacturing can result in different ranges of actuation for any two samples manufactured on the same equipment, and in similar conditions. 5) The region around the *pin-socket* interface can be affected by heat due to the laser machining process, distorting the fabricated parts. This damage can be minimized by using femtosecond laser.

Two main methods have been used to characterize interference - (I) Note the angle of actuation at which interference starts, and plot it with respect to other parameters. (II) Note the angle at which the extremity of the pin along the tube axis interferes, and plot it with respect to other parameters. The first method was accomplished by discretizing pin and socket volumes, and then numerically detecting the angle at which the volume of their intersection is non-zero, using Mathematica [26]. However, this method is seriously limited by the capabilities of Mathematica 11.1 (as of now) - some of the plots so obtained show periodic variation, indicating that the discretization is not fine enough. The second method looks at the outer surface of the pin and the inner surface of the socket. Considering only half of the pin surface split by the YZ plane, this surface is colored blue while plotting whereas the inner socket surface is colored orange. As the pin surface is rotated, at a particular angle, orange color shows through where the blue pin surface should instead end in a straight boundary. This angle is noted and the same is repeated while varying different design parameters. The drawback of this method is that it requires visual effort.

5.1 The effect of laser machining parameters

The range of the joint increases steadily with increase in $\bar{k}$ (see Fig. 5.1 (a)). This is expected, since a higher gap between the *pin* and *socket* would lead to lesser interference. The kerf width for 5mm outer diameter tubes for the samples that we have is 0.00075in (0.01905mm). The kerf width is usually constant for a particular laser setting. When this kerf width is normalized with respect to the diameter of the 5mm diameter tube, $\bar{k} = 0.000381$. But when the same kerf width is normalized with respect to the outer diameter of the 1.27mm diameter tube, then $\bar{k} = 0.015$. Hence, according to the plot in Fig. 5.1 (a) II), the 5mm diameter tube gives a range of only about $\pm 15°$, while a 1.27mm diameter tube has a range greater than $\pm 35°$, which can be considered a good range for steerable needles.

However, the range decreases with an increase in $\bar{\phi}$. This is also expected, considering that a higher kerf angle leads to a lesser gap between the *pin* and *socket* near the inner tube surface, contributing to greater interference. Decreasing ϕ from $1°$ to $0.6°$ almost doubles the range (see Fig. 5.1 (b) II).

k and ϕ are difficult to measure accurately. Even if the measurement is accurate, the assumption that the machining kerf can be completely characterized by just k and ϕ is just a simplification.

5.2 The effect of joint design parameters

A larger hinge size leads to the laser beam making a higher angle between cutting the left and right sides of the hinge (X dimension), causing a greater change in the X dimension of the *pin* and *socket* from the inner to outer surface of the tube (a greater taper). This is consistent with larger $\bar{d_h}$ hinge sizes decreasing the range of motion (see Fig. 5.1 (a) and (b), and Fig. 5.2(a) and (b)). Changing d_h from 0.5 to 0.3 increases the range by $4°$ (see Fig. 5.2(a) II)
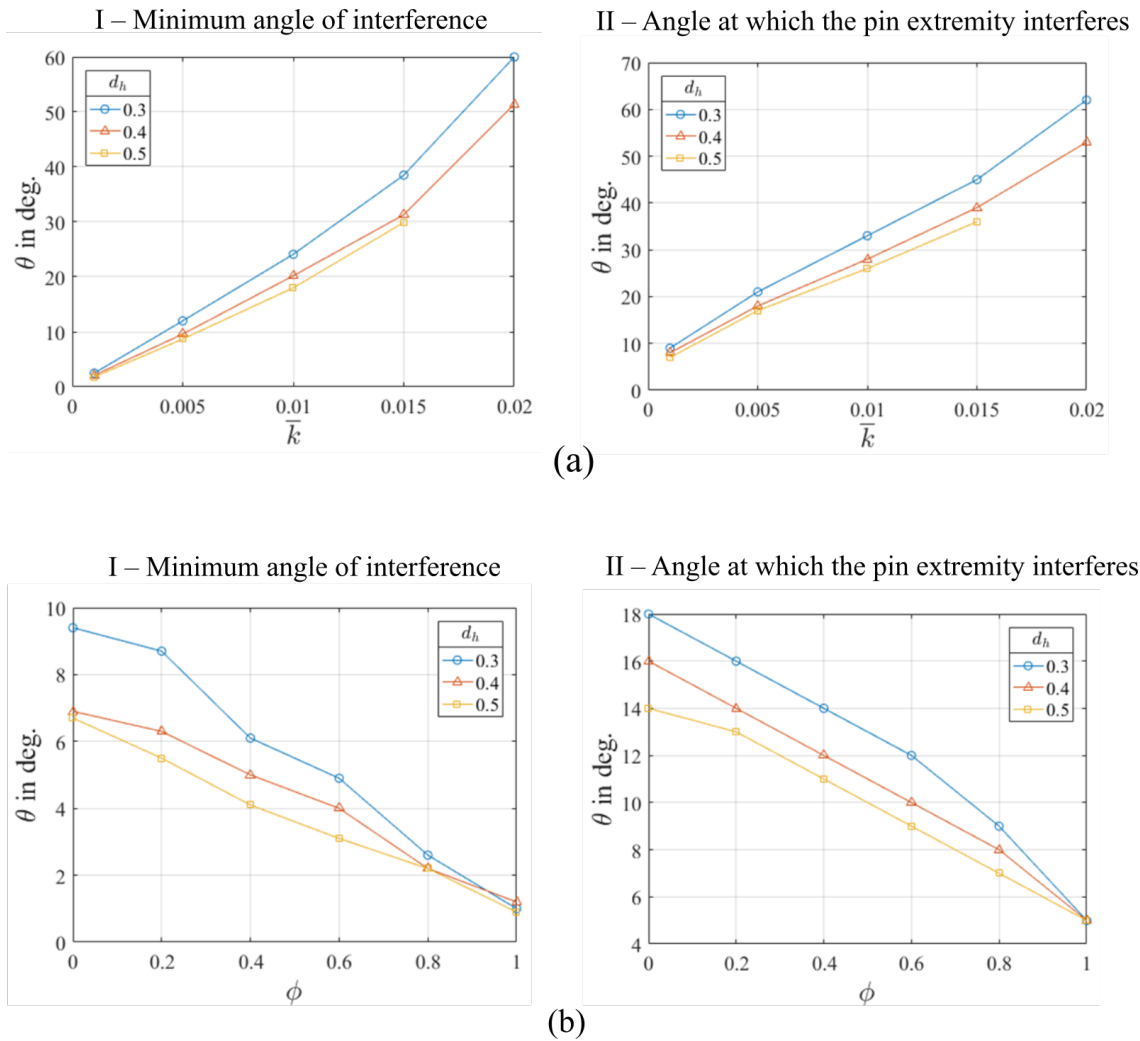
Figure 5.1: Predicted range of motion (θ_{max}) on one side, based on (a) normalized kerf size ($\overline{k}$) (where $\phi = 0°$ and $\overline{t} = 0.1$), (b) kerf angle (ϕ) (where $\overline{k} = 0.00381$ and $\overline{t} = 0.1$). (a) and (b) are estimated for normalized hinge sizes ($\overline{d_h}$) of 0.3, 0.4 and 05. Method II is generally closer to the measured range
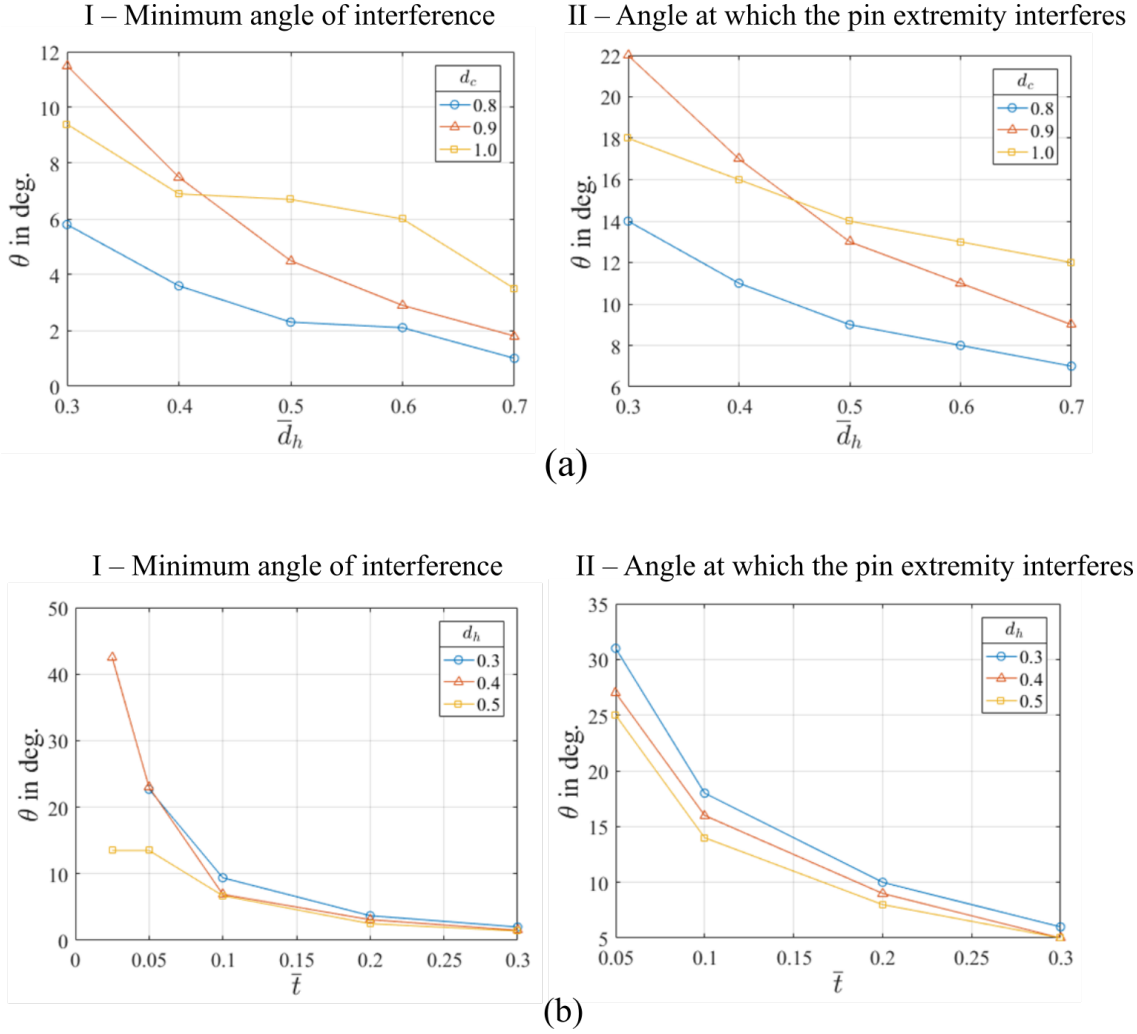
Figure 5.2: Predicted range of motion (θ_{max}) on one side, based on (a) normalized hinge size d_h for *critical section* at the inner surface ($\overline{d_c} = 0.8$), the central surface ($\overline{d_c} = 0.9$), and outer surface ($\overline{d_c} = 1$) (where $\overline{k} = 0.00381$, $\phi = 0°$, and $\overline{t} = 0.1$), (b) normalized thickness of the tubular workpiece $\overline{t}$ (where $\overline{k} = 0.00381$ and $\phi = 0°$). (b) is estimated for normalized hinge sizes ($\overline{d_h}$) of 0.3, 0.4 and 05. Method II is generally closer to the measured range
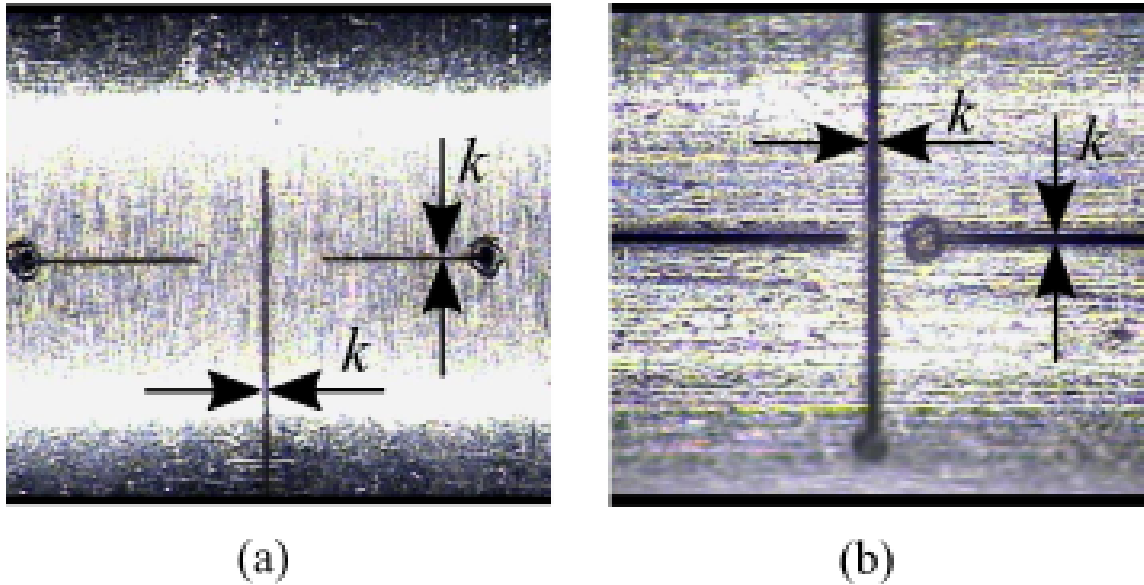
Figure 5.3: Kerf width measurements for axial and circumferential cuts on (a) 5mm diameter stainless steel tube and (b) 1.27mm diameter stainless steel tube.

5.3 The effect of workpiece parameters

A larger tube thickness ($\bar{t}$) creates more area at the *pin-socket* interface. This should decrease the range of motion for a particular fixed outer tube diameter, because the joint becomes increasingly ellipsoidal away from the critical surface. The geometric model predicts a lowering of range when the tube thickness is increased. It is notable that this effect is more pronounced at lower hinge sizes. Changing the thickness from 5% to 10% of the outer diameter can bring down the range from $\pm 25°$ to $\pm 14°$ for $d_h = 0.5$. However, when the thickness of the tube is 30% of the outer diameter, the range drops to just $\pm 5°$. (See Fig. 5.2 (b) II)

5.4 Experimental validation

Kerf size is measured using longitudinal and radial cuts (Fig. 5.3). Initially, the laser focus is adjusted till the axial and circumferential cuts are of the same size. The measure-

ment is made with respect to a known reference length on the picture (the length of the cut or the tube diameter)

Samples of normalized hinge size $d_h = 0.3$, 0.4, and 0.5 with kerf sizes $14.99\mu m$ ($\bar{k} = 0.00381$), $19.05\mu m$ ($\bar{k} = 0.003$), and $14.99\mu m$ ($\bar{k} = 0.00381$) respectively are fabricated on 5 mm diameter stainless steel tubes to avoid unwanted bending effects. These samples have two embedded orthogonal hinge joints in the $1-1$ configuration (Fig. 5.4(a), 4.2(a), and 6.1(b)). The hinge was held horizontally at the proximal end using a 3D printed holder and the tip left to hang in gravity, while each hinge is left to hang on either side. This is done for the above samples and for the four different hanging configurations of the $1-1$ hinge design (two of those hanging configurations are shown in Fig. 5.4(a)). The average of these angles is recorded. Fig. 5.4(b) shows that the predicted hinge ranges using Method II (based on the angle of interference of the pin extremity) closely follow the measured ranges of motion of the samples ($< 2°$ error).

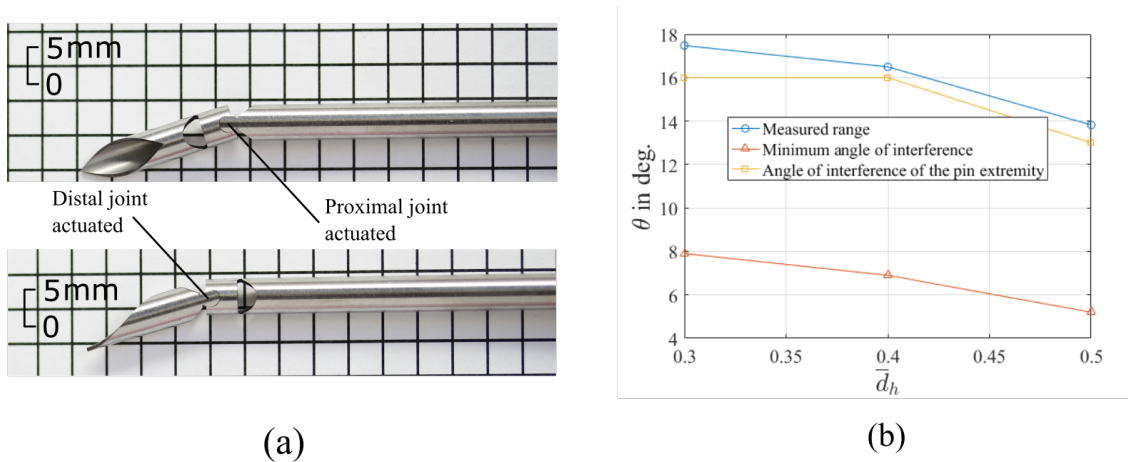(a)   (b)

Figure 5.4: (a) Hinge joint ($\overline{d_h} = 0.5$) left to actuate due to gravity in two different positions, for range measurement. (b) Predicted range of motion compared to measured ranges of motion for samples of three different hinge sizes, accounting for differing kerf widths.

There is a tradeoff between joint strength and range of motion. Increasing the hinge size can make the joint stronger against axial dislocation by providing greater support between the *pin* and the *socket*. However, it decreases the range of motion. Also, increasing the width of the neck makes the joint stronger against axial neck fracture, but reduces the range of motion.

It is to be noted that the measurements were done on 5mm diameter stainless steel tubes. The smaller sized (1.27mm diameter) stainless steel and superelastic Nitinol tubes exhibited as much range of motion as was allowed by the *neck* design. It was impractical to measure the full range of motion of such joints because at that scale, keeping the laser kerf dimensions constant, the normalized kerf width is much higher than that of the larger 5mm diameter tubes, making it easy for the joint to dislocate along its axis due to insufficient support. Due to this larger kerf gap, and due the fact that it requires much lesser force for the smaller joint to bend, the joints on smaller tubes exhibit too large a range of motion to allow a strong enough *neck* design.

The joints also exhibit an asymmetrical range of motion. This could perhaps be attributed to the way the laser machine used for the project handles the cutting process. If the joint lies at the end of the 2D sketch where the toolpaths are planned, the equipment cuts one side of the joint, rotates and translates the workpiece as it cuts other features, and finishes cutting the other side of the joint. One hypothesis is that the asymmetry in the range is because during this manipulation, the workpiece could be distorted by the interaction with the machine.

6. WORKSPACE ANALYSIS

Depending on the range of motion required, and spatial constraints, a single hinge joint may not suitable for an application. Sometimes, several hinge joints could be combined in various different configurations to effect the desired range of motion. In this section, we consider the workspace of a set of planar hinge joints and that of two orthogonal sets of hinge joints.

The axis of actuation of a hinge is defined as the local Y axis, as shown in Fig. 4.2 (a). Labeling hinges as O_i from the proximal most to the distal most in ascending order, the global origin is taken to be at $\vec{O} = O_1$. The local Z axis runs along the length of the tube segment at zero actuation. We denote homogeneous rotation matrices in the form $R_Y(\theta_i)$ (where Y denotes the axis of rotation and θ_i denotes the angle by which the rotation happens) and homogeneous translation matrices in the form $T_Z(a_i)$ (where Z denotes the axis along which translation happens and a_i is the magnitude of translation). Let $\vec{p}$ denote an arbitrary point that can be reached by the robotic system with hinges. A conservative range of actuation of $15°$ is used on either side for each hinge considering that there can be an inner tube for drug delivery.

6.1 Planar Joints

Consider the possible regions that can be reached by a planar configurations of hinges, in which all the actuation axes are parallel to one another. The workspace of such a configuration is given by:

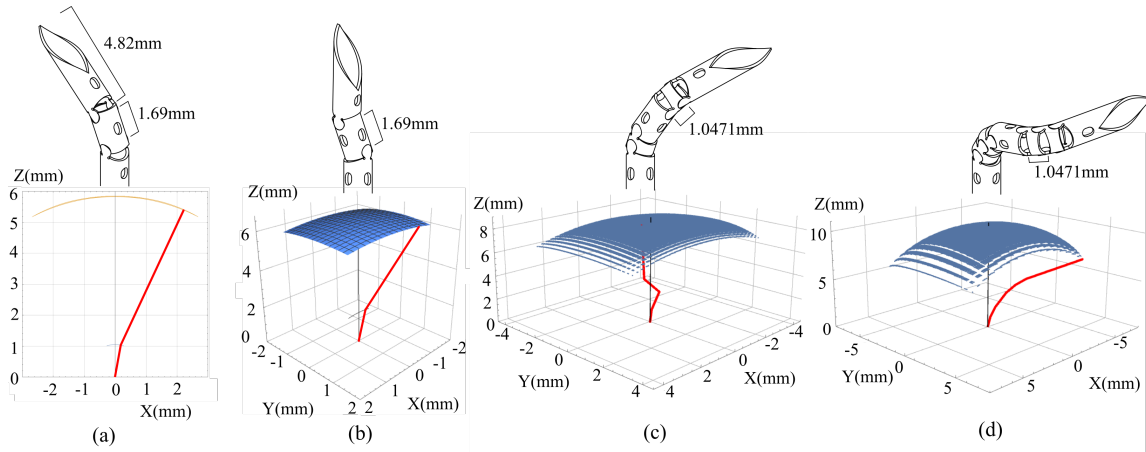$$\vec{p} = \left\{ \prod_{i=1}^{n} R_Y(\theta_i).T_Z(a_i) \right\} \vec{O}$$

Figure 6.1: Workspaces of various hinge configurations. (a)Two hinges actuating in the same plane. (b) $1-1$ orthogonal hinge configuration. (c) $2-2$ orthogonal hinge configuration. (d) $3-3$ orthogonal hinge configuration. The distal and middle tube segments have the same link lengths across the above prototypes. The red line in each plot indicates one of the possible forms of the robot

A single hinge with an end effector attached at the end of a link of length a_1 can reach points that form an arc. Adding another hinge in the same plane increases the points that the end effector can reach as seen in Fig. 6.1(a). Each of the hinges traces an arc. The combined reachable points lie on an elongated area distributed radially, like in the figure. By rotating the device about the Z axis, a larger region of points distributed about a spherical surface can be reached. But this adds to the complexity of the control system as it usually requires the actuating elements also to rotate with the device. This is especially a problem with tendon-driven joints, and can be avoided by using orthogonally embedded hinges.

6.2 Orthogonal Joints

By actuating the joints along two orthogonal axes, a device with embedded hinges can reach an ellipsoidal surface in 3D space. With rotation of the proximal end, this enables roll-pitch-yaw motion. However, to increase the bending angle, more hinges with parallel

axes can be added, making the locus of the end effector, a volume in space. For n hinges actuating along one plane and m hinges actuating along an orthogonal plane, the workspace is given by:

$$\vec{p} = \left\{ \prod_{i=1}^{n} R_Y(\theta_i).T_Z(a_i) \right\} R_Z(-\frac{\pi}{2}) \left\{ \prod_{j=1}^{m} R_Y(\theta_j).T_Z(a_j) \right\} \vec{O}$$

In the above expression, the term $\left\{ \prod_{i=1}^{n} R_Y(\theta_i).T_Z(a_i) \right\}$ arises from the proximal set of hinges in one plane and the term $\left\{ \prod_{j=1}^{m} R_Y(\theta_j).T_Z(a_j) \right\}$ emerges from the distal set of hinges in an orthogonal plane.

Let us refer to this configuration in the form- '$m-n$'. Figures 6.1 (b), (c) and (d) show the workspaces of $1-1$, $2-2$ and $3-3$ hinge configurations respectively. In the $1-1$ configuration, the device can reach points on an ellipsoidal surface. But, a device in $2-2$ or $3-3$ configuration can reach an oblate volume of points distributed about an ellipsoidal surface. There is a marked increase in the range of motion for each added hinge pair. The increased range may be desirable in certain applications, but it comes at the cost of an increased length of tube in bent configuration, which may be ill suited for tasks that are to be executed in small cavities. If the tube is underactuated, control would be imprecise, in which case having a lower number of hinges (and hence segments) would result in a better outcome. In any case, it is advantageous to decrease the length of tube segments between the hinges, as it leads to more efficient use of the workspace.

7. CONCLUSIONS AND FUTURE WORK

In this thesis, we introduce a method for the design and fabrication of laser-machined, embedded hinge joint on tubular devices, while preserving the inner channel. The joint does not need assembly and is secured in place due to the wedging action created due to on-axis machining. We present a geometric model of the joint, incorporating the ellipsoidal nature of the components. We then use the model to predict the range of motion for the joints embedded on rigid tubes based on variation of the joint design parameters, the workpiece geometry, and the laser machining parameters. The predicted range of motion was compared to the measured values for fabricated samples of different hinge sizes and kerf dimensions, and it was shown that the predicted values are close to the measured ranges across samples. We also present the different configurations of these hinge joints to achieve differing degrees of usable workspace. The embedded hinge joints described in this thesis could be used for micro-robotic applications and minimally invasive surgical devices for neurosurgery and pediatric surgery. In the future, we plan to examine various tendon routing methods, the kinematics of tendon actuation and the mechanical strength of the joints.

REFERENCES

[1] S. P. DiMaio and S. Salcudean, "Needle steering and motion planning in soft tissues," *IEEE Transactions on Biomedical Engineering*, vol. 52, no. 6, pp. 965–974, 2005.

[2] R. J. Webster, J. S. Kim, N. J. Cowan, G. S. Chirikjian, and A. M. Okamura, "Nonholonomic modeling of needle steering," *The International Journal of Robotics Research*, vol. 25, no. 5-6, pp. 509–525, 2006.

[3] S. Misra, K. B. Reed, B. W. Schafer, K. Ramesh, and A. M. Okamura, "Mechanics of flexible needles robotically steered through soft tissue," *The International journal of robotics research*, 2010.

[4] S. I. Seldinger, "Catheter replacement of the needle in percutaneous arteriography: a new technique," *Acta radiologica*, vol. 39, no. 5, pp. 368–376, 1953.

[5] S. C. Ryu, Z. F. Quek, J.-S. Koh, P. Renaud, R. J. Black, B. Moslehi, B. L. Daniel, K.-J. Cho, and M. R. Cutkosky, "Design of an optically controlled mr-compatible active needle," *IEEE Transactions on Robotics*, vol. 31, no. 1, pp. 1–11, 2015.

[6] P. A. York, P. J. Swaney, H. B. Gilbert, and R. J. Webster, "A wrist for needle-sized surgical robots," in *Robotics and Automation (ICRA), 2015 IEEE International Conference on*, pp. 1776–1781, IEEE, 2015.

[7] T. K. Adebar, J. D. Greer, P. F. Laeseke, G. L. Hwang, and A. M. Okamura, "Methods for improving the curvature of steerable needles in biological tissue," *IEEE Transactions on Biomedical Engineering*, vol. 63, no. 6, pp. 1167–1177, 2016.

[8] P. J. Swaney, J. Burgner, H. B. Gilbert, and R. J. Webster, "A flexure-based steerable needle: high curvature with reduced tissue damage," *IEEE Transactions on Biomedical Engineering*, vol. 60, no. 4, pp. 906–909, 2013.

[9] N. Shahriari, R. J. Roesthuis, N. J. van de Berg, J. J. van den Dobbelsteen, and S. Misra, "Steering an actuated-tip needle in biological tissue: Fusing fbg-sensor data and ultrasound images," in *Robotics and Automation (ICRA), 2016 IEEE International Conference on*, pp. 4443–4449, IEEE, 2016.

[10] A. J. Petruska, F. Ruetz, A. Hong, L. Regli, O. Sürücü, A. Zemmar, and B. J. Nelson, "Magnetic needle guidance for neurosurgery: Initial design and proof of concept," in *Robotics and Automation (ICRA), 2016 IEEE International Conference on*, pp. 4392–4397, IEEE, 2016.

[11] F. Jelínek, E. A. Arkenbout, P. W. Henselmans, R. Pessers, and P. Breedveld, "Classification of joints used in steerable instruments for minimally invasive surgeryâĂŤa review of the state of the art," *Journal of Medical Devices*, vol. 9, no. 1, p. 010801, 2015.

[12] D. A. Parrott, B. T. Krupp, C. L. Gillum, C. J. Matice, and L. P. Mingione, "Articulating laparoscopic surgical instruments," May 3 2012. US Patent App. 12/916,142.

[13] B. Blase, "Articulated section of a shaft for an endoscopic instrument," Apr. 20 2016. EP Patent 2,438,844.

[14] M. Banik, D. Boulais, J. Couvillon, A. Chin, F. Anderson, F. Macnamara, S. Fantone, D. Braunstein, D. Orband, M. Saber, *et al.*, "Articulation joint," Dec. 24 2014. EP Patent 2,617,350.

[15] F. Shelton and M. Ortiz, "Articulatable surgical device with rotary driven cutting member," Nov. 15 2016. US Patent 9,492,167.

[16] R. D. Brunnen and T. J. Simon, "Bendable portion of an insertion tube of an endoscope and method of producing it," Aug. 3 2010. US Patent 7,766,821.

[17] T. Cooper, "Surgical instrument with parallel motion mechanism," May 17 2011. US Patent 7,942,868.

[18] N. T. Berlinger, "Robotic surgery-squeezing into tight places," *New England Journal of Medicine*, vol. 354, no. 20, pp. 2099–2101, 2006.

[19] N. E. Bruns, O. S. Soldes, and T. A. Ponsky, "Robotic surgery may not âĂIJmake the cutâĂİ in pediatrics," *Frontiers in pediatrics*, vol. 3, 2015.

[20] D. E. Dolmans, D. Fukumura, and R. K. Jain, "Photodynamic therapy for cancer," *Nature reviews cancer*, vol. 3, no. 5, pp. 380–387, 2003.

[21] M. Laroussi, "From killing bacteria to destroying cancer cells: 20 years of plasma medicine," *Plasma Processes and Polymers*, vol. 11, no. 12, pp. 1138–1141, 2014.

[22] R. Pardal, M. F. Clarke, and S. J. Morrison, "Applying the principles of stem-cell biology to cancer," *Nature Reviews Cancer*, vol. 3, no. 12, pp. 895–902, 2003.

[23] S. B. Alapati, W. A. Brantley, T. A. Svec, J. M. Powers, J. M. Nusstein, and G. S. Daehn, "Sem observations of nickel-titanium rotary endodontic instruments that fractured during clinical use," *Journal of Endodontics*, vol. 31, no. 1, pp. 40–43, 2005.

[24] P. Parandoush and A. Hossain, "A review of modeling and simulation of laser beam machining," *International Journal of Machine Tools and Manufacture*, vol. 85, pp. 135–145, 2014.

[25] R. Pfeifer, D. Herzog, M. Hustedt, and S. Barcikowski, "Pulsed nd: Yag laser cutting of niti shape memory alloysâĂŤinfluence of process parameters," *Journal of Materials Processing Technology*, vol. 210, no. 14, pp. 1918–1925, 2010.

[26] Wolfram Research, Inc., "Mathematica 11.1."